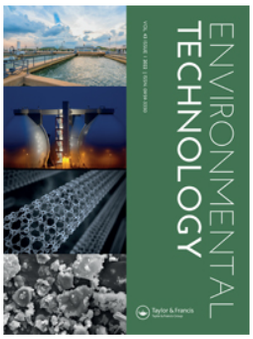

Environmental Technology

ISSN: 0959-3330 (Print) 1479-487X (Online) Journal homepage: www.tandfonline.com/journals/tent20

Microwave-assisted hydrothermal synthesis of MoS_2–Ag_3PO_4 nanocomposites as visible light photocatalyst for the degradation of tetracycline hydrochloride

Hnin May Lwin, Weiquan Zhan, Feifei Jia & Shaoxian Song

To cite this article: Hnin May Lwin, Weiquan Zhan, Feifei Jia & Shaoxian Song (2022) Microwave-assisted hydrothermal synthesis of MoS_2–Ag_3PO_4 nanocomposites as visible light photocatalyst for the degradation of tetracycline hydrochloride, Environmental Technology, 43:1, 149-162, DOI: 10.1080/21622515.2020.1782478

To link to this article: https://doi.org/10.1080/21622515.2020.1782478

Published online: 14 Jul 2020.

ENVIRONMENTAL TECHNOLOGY
2022, VOL. 43, NO. 1, 149–162
https://doi.org/10.1080/21622515.2020.1782478

Taylor & Francis
Taylor & Francis Group

Microwave-assisted hydrothermal synthesis of MoS_2–Ag_3PO_4 nanocomposites as visible light photocatalyst for the degradation of tetracycline hydrochloride

Hnin May Lwin[a,b], Weiquan Zhan[a], Feifei Jia[a] and Shaoxian Song[a]

[a]Hubei Key Laboratory of Mineral Resources Processing and Environment, Wuhan University of Technology, Wuhan, People's Republic of China; [b]Department of Industrial Chemistry, West Yangon University, Yangon, Myanmar

ABSTRACT

In the modern era, industrialization has facilitated the human life but produced several severe pollutants as well that are hazardous in nature. Thus the degradation of these hazardous material has drawn considerable attention. This study deals with the synthesis of MoS_2/Ag_3PO_4 heterojunction nanocomposite with 1–50% wt. using a microwave-assisted hydrothermal process as well as photocatalytic activity of tetracycline hydrochloride (TCH) degradation has been analysed. The compositional properties of nanocomposite catalysts have been studied through X-ray diffraction, Fourier transform infrared, X-ray photoelectron spectroscopy as well as structural and morphological studies were conducted through scanning electron microscopy, transmission electron microscopy, Brunauer–Emmet–Teller, photoluminescence, N_2 physical adsorption, UV–vis diffuse reflectance spectroscopy. This provides an excellent and efficient mechanism for the remediation of residual organic contaminants under visible light that could be used to decontaminate the atmosphere.

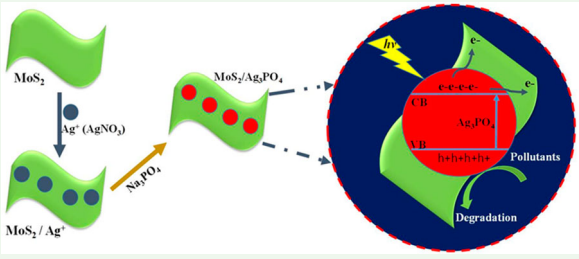

ARTICLE HISTORY
Received 27 March 2020
Accepted 5 June 2020

KEYWORDS
Heterojunction; molybdenum disulphide; silver orthophosphate; visible light irradiation; tetracycline antibiotics

1. Introduction

Industrial development in the contemporary world has carried out the growth of innovative products, but it has produced new pollutants that may seriously damage our environment [1,2]. Contaminants from biological species and chemicals have severely affected the environment and living species [3], furthermore exacerbating the fresh water disaster in several developing countries. Drug antibiotics are one of the most commonly used drugs in medical treatments and agriculture production and are often found in soil, underground water, at the surface of water and even in the drinking water. Since various chemicals including pesticides, antibiotics, heavy metals and toxins are not efficiently removed in the water treatment processes, which pose serious threat to human health. Tetracycline hydrochloride (TCH), a major group of global antibiotics, is recurrently detected in sediments, surface waters and ground waters in current years due to the stable chemical structure and recalcitrance to biological degradations. It may act as a principal disruptor of soil respiration, reduction (ferric), and nitrification and phosphatase activities. Furthermost, antibiotics are not completely metabolized and absorbed by animals as well as humans [4–6]. Certain antibiotics that are used in excess have low biodegradability and may cause various adverse effects, together with acute and chronic toxicity, damage to aquatic photosynthetic organisms' effects on local microbial populations, and destruction to drug resistance genes in microorganisms [7,8]. Therefore, residues of antibiotic in water establish life-threatening hazards to human and environment, which are the foremost challenges [9]. Conventional water treatment systems filtered out microorganism on the other hand waste water cannot completely remove antibiotics [10]. Therefore, life-threating risks to human

CONTACT Feifei Jia feifeijia@whut.edu.cn Hubei Key Laboratory of Mineral Resources Processing and Environment, Wuhan University of Technology, Luoshi Road 122, Wuhan, Hubei, 430070, People's Republic of China

and environment as well as economic losses have distended the urgency to improve the operative and state-of-the-art technologies to completely eliminate antibiotics from water, especially from drinking water [11,12].

Owing to their potential applications in the field of hydrogen evolution reaction and in the elimination of organic pollutants and contaminants from the environment, semiconductor photocatalysts have attracted considerable attention in recent years [13–15]. Although, TiO_2 is a semiconductor material that has been most widely studied since the discovery of TiO_2 as a photoelectrode. However, maximum efficiency of TiO_2 is restricted simply for a UV light region because of its significant band gap energy of 3.2 eV. There have been several approaches to extend the performance of photocatalytic semiconductors from UV to visible light [16]. In addition to the TiO_2-based photocatalysts, a number of investigations on the enhancement of visible light photocatalysis of other potential semiconductor metal oxides, carbides, phosphides, ferrites, dichalcogenides, nitrides, oxynitrides, etc. have been studied in recent years [17–22]. In general, the optimization of band structures by doping metallic or non-metallic elements, decoration of metallic nanoparticles like Pt, Au and Ag on the surface of semiconductor, morphology tuning, and construction of heterostructures or composites are the major techniques performed in conventional photocatalysts to make them visible light active [23–26].

By integrating semiconductor nanoparticles with good distribution, the performance characteristics of MoS_2 sheets can be enhanced. Nanoparticles decorated MoS_2 sheets can develop specific synergetic characteristics. MoS_2 nanosheets have recently been documented, were decorated with semiconductor nanoparticles. Heterostructured catalysts, in comparison with individual catalyst, have better performance and have been proved more efficient [27–36].

Among the most challenging problems for heterostructured photocatalysts is to find specific materials with both a high photocatalytic activity and a reduced recombination effect for the degradation of pollutants. MoS_2 nanosheets with well-dispersed nanoparticles in semiconductor can provide greater flexibility for selective catalysis and transportation of charge carriers. This results in the increased porosity and large specific surface area of semiconductor nanocomposites materials. Therefore, Ag_3PO_4 decorated with composites MoS_2 can offer innovative opportunities to improve new photocatalyst materials.

Keeping the literature review and to best of our understanding, there exist no reports on the Ag_3PO_4 synthesis integrated as photocatalyst MoS_2 ultrathin nanosheets. Thus, in this study, we introduced two-steps method and used it as a photocatalyst. Apart from its unique electronic properties, layered MoS_2 possesses large theoretical specific surface area and excellent chemical stability. Hence, in this study, a composite material of MoS_2 with different wt.% of highly photoactive Ag_3PO_4 was fabricated via microwave hydrothermal process and evaluated using physicochemical properties, photocatalytic activity and performance of the photocatalyst composite.

2. Experimental procedure

All chemical elements were of analytical grade and used without any additional purification.

2.1. Preparation of MoS_2 ultrathin nanosheets

Generally, 2 mmol $(NH_4)_6Mo_7O_{24}{\cdot}4H_2O$ and 0.06 M thiourea were dissolved under intense stirring in 70 mL distilled water to develop a homogeneous solution. Thereafter, solution was shifted to a 100-mL Teflon-lined stainless steel autoclave after being stirred for 30 min and kept for 24 h at 200°C. The reaction mechanism was further cool down naturally in order to reach at room temperature. The collected material was processed via centrifugation, cleaned using distilled water and ethanol and finally dried under vacuum at 60°C.

2.2. Preparation of MoS_2 ultrathin nanosheets decorated with Ag_3PO_4 nanoparticle

For a typical synthesis of MoS_2/Ag_3PO_4 composite, at first, 200 mg of MoS_2 was dispersed in 40 mL of distilled water. Then, it was sonicated for 1 h to obtain the dispersed MoS_2 nanosheets. Then, 0.12 M of $AgNO_3$ was added into it under vigorous stirring. In the second beaker, 0.12 M of Na_2HPO_4 was dissolved in 40 mL of distilled water, and the solution was poured dropwise into the first beaker containing $AgNO_3$ solution and dispersed MoS_2 under constant stirring. The mixture was then transferred into a Teflon vessel for the microwave hydrothermal treatment at 150°C for the period of 1 h. The obtained precipitate was separated by centrifuge followed by several times of washing with distilled water and ethanol. Then, the subsequent product was air dried overnight at 60°C in order to remove moisture. The composite products of MoS_2 with 1, 3, 5, 7, 10, 30 and 50% wt. of Ag_3PO_4 were labelled as MAP-1, MAP-2, MAP-3, MAP-4, MAP-5, MAP-6 and MAP-7, respectively. For evaluation purposes, pure Ag_3PO_4 was also synthesized without the addition of MoS_2.

2.3. Characterization of samples

The structural characteristics of the attained precipitates were studied using (XRD) X-ray diffraction with Cu-Kα radiation by means of a Shimadzu Labx XRD 6100. The size and morphologies of synthesized samples were carried out through Field-Emission Scanning Electron Microscope (FESEM, JEOL-6300F). Transmission electron microscope (TEM, Hitachi H-7000) having 110 kV (volt) and a high-resolution TEM (HRTEM, Tecnai G2 F 20 S-Twin TEM) at an operating acceleration voltage of 210 kV (volt) were used to analyse nanoparticles. FTIR (Fourier transform infrared spectroscope, Avatar 370) with a spectral range (400–4000 cm^{-1}) and XPS (X-ray photoelectron spectroscopy, Thermo Scientific K-alpha surface analysis instrument) were used to investigate the purity of final product. Specific surface areas of adsorption–desorption method at 77 K (Micrometrics Tristar ASA 3000) using Brunauer–Emmett–Teller (BET) method and UV–vis diffuse reflectance spectra (UV–vis DRS) were obtained for the dry-pressed disk samples using a UV–vis spectrometer (UV-2450, Shimadzu, Japan). $BaSO_4$ was used as a reflectance standard in UV–vis diffuse reflectance experiments. The photoluminescence (PL) spectrum was obtained using Fluorescence spectrophotometer (Hitachi F-4500) having Xe lamp as the excitation source, and excitation wavelength of 210 nm was used. Electrochemical impedance spectroscopy measurements (PC and EIS) were carried out using electrochemical working station (CHI 660D, CH Instruments, Inc., Shanghai). The platinum wire SCE (saturated calomel electrode), working electrode, and reference electrode FM/A-6%, were used, respectively. Throughout experiment, the range of frequencies 10 −5 Hz and 10−2 Hz was adjusted with initial voltage of −0.01 V (volt) in 0.01 mol/ Na_2SO_4 aqueous solution to record the EIS analysis. A light source was used for the measurement of photocurrent (PC) with 500 W Xe lamp and an aqueous solution of 0.5 mol/L Na_2SO_4.

2.4. Evaluation of photocatalytic performance

Photocatalytic studies were carried out at normal pH of a TCH solution, an organic pollutant. The experimentation complicated a photo reactor having a 300-W mercury lamp used as an internal light source having a main emission wavelength of 420–780 nm, enclosed with a quartz vessel. The initial pH of TCH solution was 3.96, without adjustment during the photo catalysis process. The light source is enclosed by means of a suspension of Ag_3PO_4 decorated MoS_2 nanosheet catalyst and aqueous TCH (100 mL, 1 g/L). The suspension was stirred for 30 min before irradiation in the dark environment to ensure a good dispersion and to obtain an adsorption–desorption equilibrium within the organic pollutant molecules and catalyst. The reaction solution samples were collected at specific time intervals during light irradiation and analysed with an optical spectrophotometer.

3. Results and discussion

3.1. X-Ray diffraction (XRD) analysis

The XRD characteristics of pure MoS_2, Ag_3PO_4 and MoS_2/Ag_3PO_4 heterojunctions with distinct Ag_3PO_4 contents are shown in Figure 1. The cubic phase of Ag_3PO_4 (JCPDS card no. 06-0505) could be obviously appointed to all the diffraction peaks in bare Ag_3PO_4 patterns. All peaks in violent line were categorized through the presence of Bragg diffraction planes at an angle $2\theta = 21.0°$, 29.8°, 33.4°, 36.7°, 47.9°, 52.8°, 55.1°, 57.3°, 61.7° and 73.9° which are indexed to (110), (200), (210), (211), (310), (222), (320), (321), (400) and (332) planes of body-centred cubic structure of Ag_3PO_4, respectively. In the case of pure MoS_2, orthorhombic phase of MoS_2

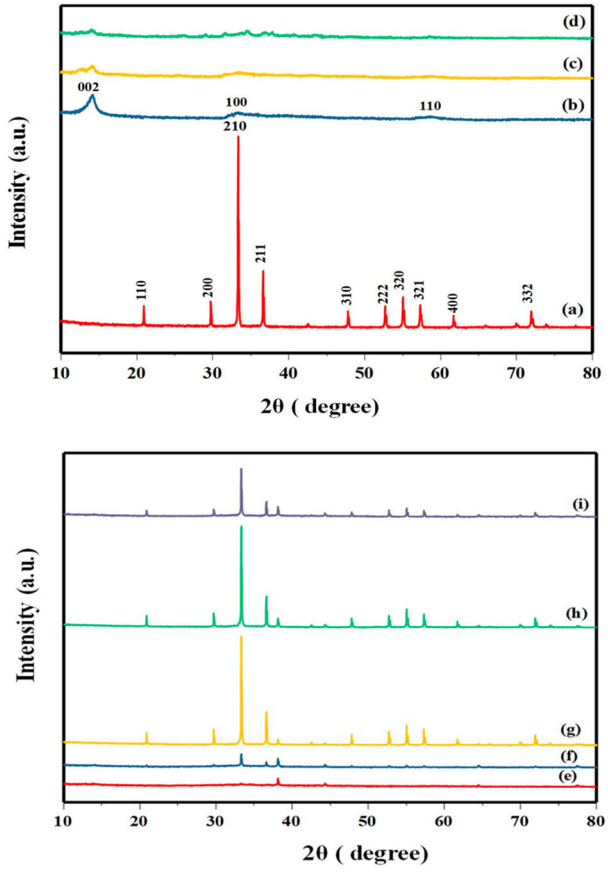

Figure 1. XRD patterns of (a) Ag_3PO_4, (b) MoS_2, (c) MAP-1, (d) MAP-2, (e) MAP-3, (f) MAP-4, (g) MAP-5, (h) MAP-6 and (i) MAP-7 photocatalysts.

(JCPDS card no.37-1497) the peaks at an angle $2\theta = 14°$, 33° and 58.4° could be allocated to the (002), (100) and (110) planes, respectively [37–39]. Hence, from the XRD patterns, it is clear that the synthesized samples contain MoS_2 and Ag_3PO_4 with good crystallinity. Additional peaks were not detected for any other impurities.

3.2. XPS analysis

XPS measurements further describe the elemental composition and chemical states of the MAP-6 composite. The findings are shown in Figure 2, which shows the concentrations of Ag, Mo, S, P, C and O. No peaks are observed which correspond to other elements. The high-resolution Ag 3d spectrum (Figure 2b) can be tailored to two peaks, and the binding energies at 367.8 and 374.45 eV. It can be attributed, respectively, to Ag $3d_{5/2}$ and Ag $3d_{3/2}$, which indicate the existence of Ag^+. The Mo 3d XPS spectrum high resolution as in Figure 2(c) indicates the binding energies of 231.8 eV for Mo $3d_{5/2}$ and 227.3 eV for Mo $3d_{3/2}$, proposing that Mo is in the oxidation state $^{4+}$. The S 2p XPS band (Figure 2d) can be split into two peaks placed at 160.8 and 161.6 eV, referring to the S $2p_{3/2}$ and S $2p_{1/2}$ in the MoS_2, respectively [40]. In P 2p XPS spectrum as in Figure 2(e) broad peak having binding energy 131.5 eV, which belongs to the P^{5+} in the Ag_3PO_4 material. The presence of the C 1s peak (Figure 2f) is positioned at 283.7 eV and is due to the generally adventitious XPS instrument hydrocarbons themselves. The O 1s spectrum (Figure 2g) can be tailored into two peaks positioned at 529.0 and 531.5 eV, respectively, arising from O^{2-} in the Ag_3PO_4 and the hydroxyl group.

3.3. Morphologic characterization

3.3.1. SEM and TEM analyses

SEM images as in Figure 3 show the morphologies of the samples as-prepared. Using Figure 3(a), as-synthesized Ag_3PO_4 products have an asymmetrical polyhedron crystal structure and, having dimension of about 1–5 µm in scale, and some of small particles are scattered round large particles. Hydrothermally synthesized MoS_2 material SEM images as in Figure 3(b) indicate that the ultrathin nanosheets are shown on stripped MoS_2. The certain aggregation of the stripped MoS_2 layer-like material and MoS_2 materials was not reduced to parts. As shown in Figure 3(c), Ag_3PO_4 particles are distributed evenly without obvious agglomeration over the MoS_2 ultrathin nanosheets. Furthermore, there is a slight decrease in the particle size of Ag_3PO_4 in MAP-6 and a uniform decrease when a particular quantity of MoS_2 was hybridized with Ag_3PO_4, which indicates that, adding Ag_3PO_4 has an impact on the particle size of MoS_2 ultrathin nanosheets. The chemical composition of MAP-6 nanocomposite was investigated by EDS (energy dispersive X-ray analysis). It is observed that in Figure 3(d) the elemental mapping images expose the existence of Mo, P, Ag and O, distributed uniformly all the way through the sample with S alongside. as in Figure 3(d). Figure 3 displays the EDS spectrum used for numerical investigation of the comparative atomic percent is sum-up in the table of Figure 3(d). The comparative atomic ratio replicates the nanocomposite's elemental composition, in which it is estimated to be 1.2:3.17:40.1:10.5:1.0 for a ratio of Mo:P:Ag:O:S. These values coincident well with the relative area ratio of the elements through XPS analysis. Ag_3PO_4, MoS_2 and MAP-6 photocatalyst TEM images are shown in Figure 4(a)–(c). These images authenticated that the Ag_3PO_4 particles are accumulated on the MoS_2 ultrathin nanosheets. Figure 4(d) showed clearly that the lattice fringes at 0.59 and 0.27 nm, which relates to the (002) of MoS_2 and (210) planes of pure Ag_3PO_4, respectively. The sizes and morphology of as-prepared MoS_2 have been characterized by SEM (shown in Figure 3b). Figure 4(b) shows that the as-synthesized MoS_2 ultrathin nanosheets have uniform fibre-like morphology with diameters of about 0.2 µm, which are regularly stacked by many MoS_2 sheets. In addition, with higher magnification, as shown in Figure 4(c), MoS_2 nanosheets are constructed of lump-like structures with Ag_3PO_4 and there are many interspaces among the lump. Obviously, this kind of structure has the higher specific surface area, which promises potential applications as catalyst. These results suggest it plays crucial role on the formation of MAP-6 photocatalyst in the heterojunction. It shows clearly that MoS_2 and Ag_3PO_4 have well-mixed composite heterojunctions, which are capable of improving the separation of the charge and effective movement of electrons within structure compared with pure Ag_3PO_4 and MoS_2 ultrathin nanosheets.

3.3.2. BET analysis

In photocatalytic degradation of organic contaminants, the specific surface area is a vital parameter as it affects active site numbers as well as adsorption efficiency of the material. Consequently, specific surface area of samples was measured using Brunauer–Emmett–Teller (BET) characterization. The pore size distribution (PSD) of Ag_3PO_4, MoS_2 and MAP-6 as well as corresponding N_2 adsorption–desorption isotherm have been shown in Figure 5. The N_2 adsorption–desorption isotherms acquired for three samples (curve a, b and c) are type IV in accordance with IUPAC and show significant P/P0

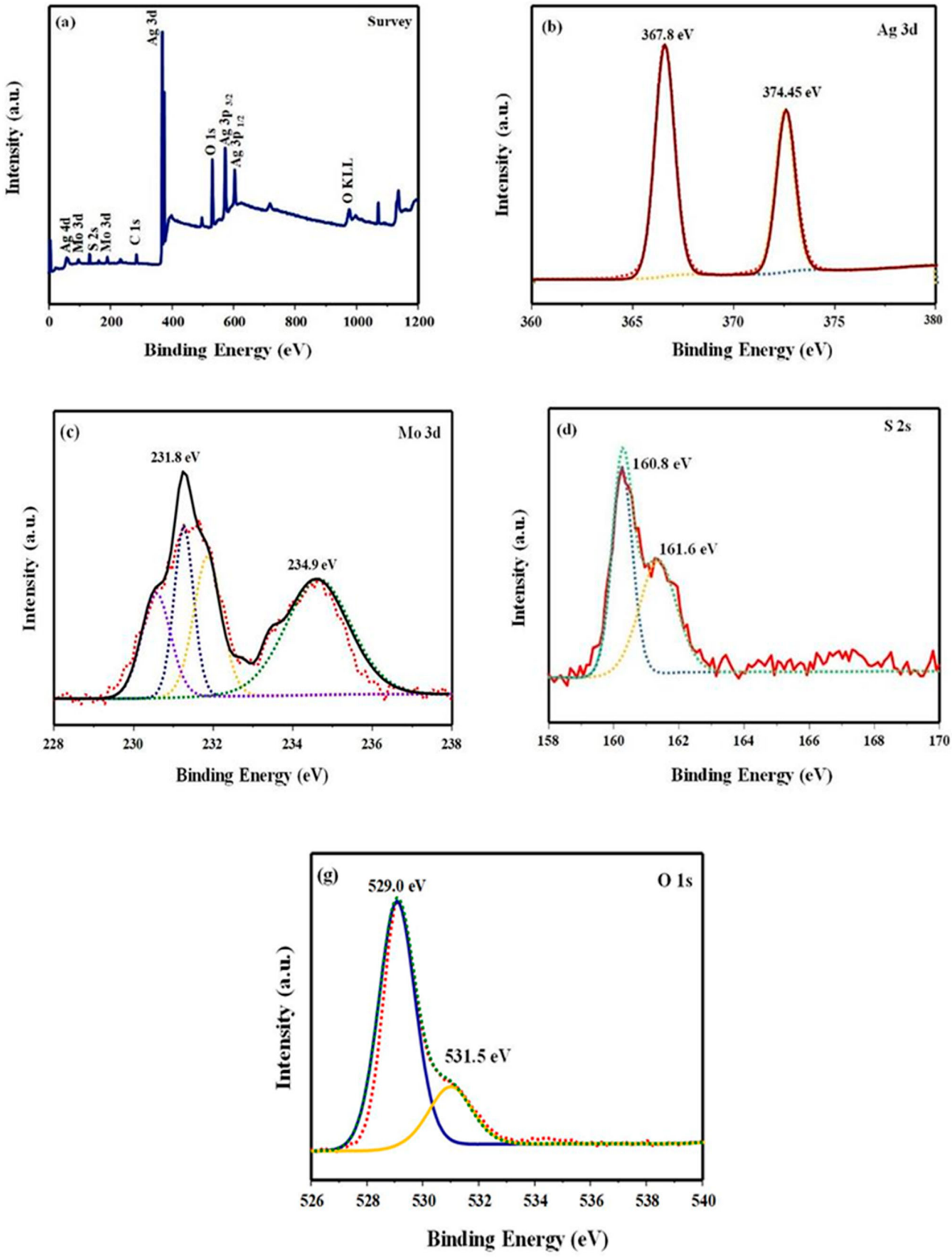

Figure 2. XPS spectra of MAP-6 photocatalyst: (a) survey, (b) Ag 3d, (c) Mo 3d, (d) S 2s, (e) P 2p, (f) C 1s, (g) O 1s.

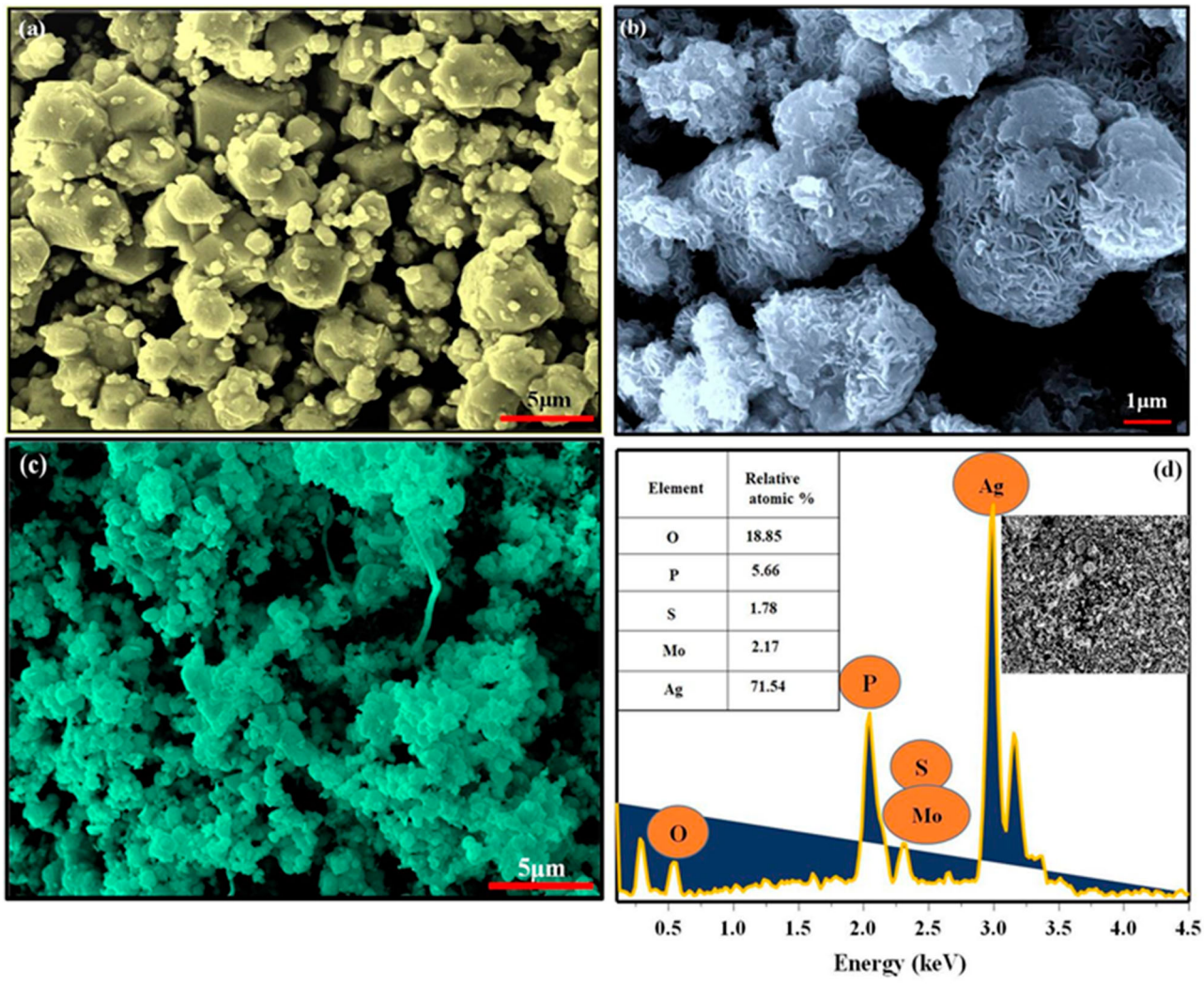

Figure 3. (a) SEM image of pure Ag_3PO_4, (b) SEM image MoS_2 ultrathin nanosheets, (c) SEM image of MAP-6 photocatalyst and (d) EDS spectrum of MAP-6 photocatalyst.

relative pressure hysteresis from 0.1 to 1.0. To conduct specific surface area in relative pressure (P/P0) resulting ranging from 0.01 to 0.99, BET multipoint technique was used. The specific surface area of pure Ag_3PO_4 is 0.33 m^2/g, low as compared to MoS_2 that has 7.02 m^2/g which shows a smaller specific surface area of 0.33 m^2/g and MoS_2 is 7.02 m^2/g. However, significant advantage was found when Ag_3PO_4 distributed upon the surface of MAP-6, subsequent, specific surface area of MAP-6 increases to 0.84 m^2/g. The Barrett–Joyner–Halenda (BJH) method has been used to verify PSD of the samples. The Ag_3PO_4, MoS_2 and MAP-6 PSD images were added to Figure 5 (a1, b1, c1), as well as 2.21, 1.72 and 2.65 nm are the pore diameters, respectively. The increment in specific surface area of the nanoparticles is based upon the partial mesoporous structure. It was making it useful to improve diffusion organic contaminants molecules, whereas this kind of porous structures comprise effective passage to the reactants as well as for products.

3.3.3. UV–Vis DRS analysis

The optical characterization of as-prepared samples was carried out using UV–Vis DRS. As shown in Figure 6, the fundamental absorption edge of pure Ag_3PO_4 is at 537 nm. The MoS_2 absorption edge is occurred at around 648 nm. Definitely, it is figured out that absorption intensity of MAP-6 increased in the visible region after combined with MoS_2. Obviously, the absorption band edges of the composite shift toward the long wavelength are increasing as the MoS_2 contents, namely 'the blue shift' conduct. Significantly, the semiconductor band gap can be determined with mentioned formula as: $ah\upsilon = C\,(h\upsilon\text{-}E_g)^{n/2}$, where a, h, υ, E_g and C are absorption coefficient, Planck constant, light frequency, band gap energy and proportionality constant, respectively.

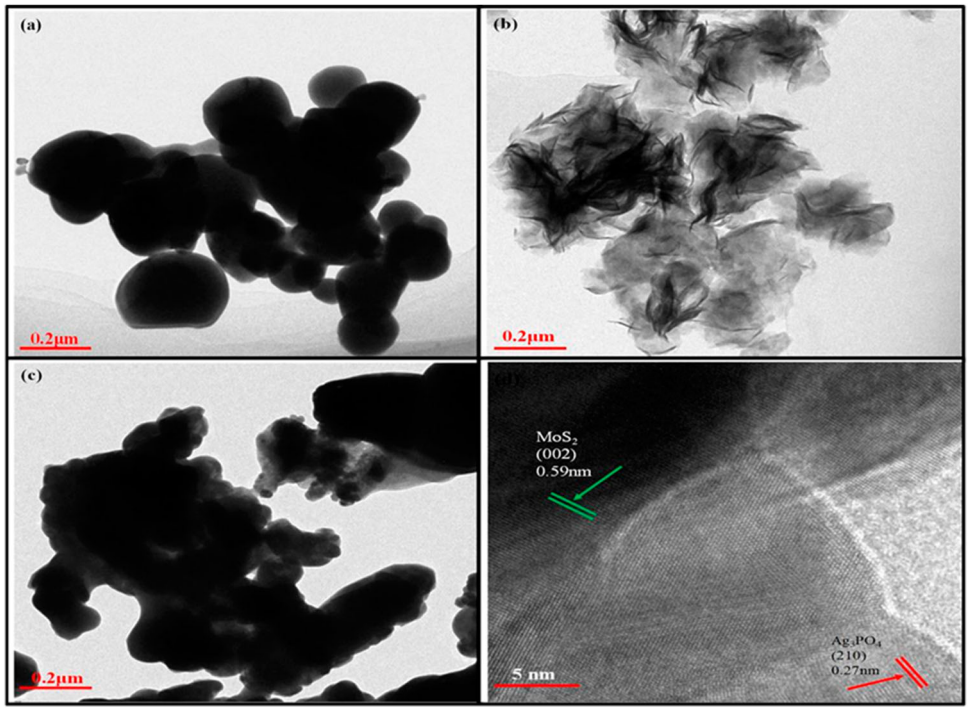

Figure 4. TEM images of (a) pure Ag_3PO_4, (b) MoS_2 ultrathin nanosheets, (c) MAP-6 photocatalyst, (d) HRTEM image of MAP-6 photocatalyst.

The magnitude of n is based upon the nature of a semiconductor material. Specifically, for direct band gap semiconductor $n = 1$ whereas for indirect band gap material $n = 4$. Hence, according to Equation (1), in view of the direct band gap for 3 samples, Figure 7 provides the plots of $(ah\upsilon)^2$ versus $h\upsilon$. As a matter of fact, E_g values for Ag_3PO_4, MoS_2 and MAP-6 photocatalyst are 2.22, 1.82 and 2.54 eV, respectively, through a liner fitting.

3.3.4. Photoelectrochemical performance

In semiconductor materials, photocatalytic activity is generally based upon the photogenerated charges separation at the interface. Photocatalytic substance performance plays an important role in semiconductors for the separation efficiency and transmission of electron–hole pairs. A typical characterization technique such as EIS was used for searching interface separation efficiency of photogenerated charges. The EIS Nyquist plot for MAP-6 composite and Ag_3PO_4 and MoS_2 nanoparticles is shown in Figure 8. The behaviour between interface layer and electrode surface can be described as the arc radius in the EIS Nyquist graph. The reduced arc radius represents low impedance and the carrier transmitting mechanism thus represents the more effective interface. Figure 8 shows that small arc radius of MAP-6 owns larger efficiency in charge electron transfer and separation as compared to pure MoS_2 and Ag_3PO_4 nanoparticles. The results showed in Figure 8 definitely demonstrate that MoS_2 and Ag_3PO_4 should promote the efficiency of MAP-6 composite charge separation, therefore, allow it to have an enhanced photocatalytic activity.

3.3.5. FTIR analysis

Figure 9 shows Fourier transform infrared (FTIR) spectroscopy characterization of MoS_2, Ag_3PO_4 and MAP-6 composite photocatalyst. For curve (a), the P–O stretching vibration in PO_4 was allocated to the two peaks one is at 1010 cm^{-1} and other at 1010 cm^{-1} in the Ag_3PO_4 FTIR spectrum. The bands can be attributed to the bending and stretching of H–O in the water adsorbed over its surface at 1381 and 1659 cm^{-1}. The bands could be linked to the bending and stretching of the hydrogen bond in the water at 2282 and 3225 cm^{-1}. Curve (b) demonstrates the MoS_2 nanosheet spectra of the FTIR. Absorption bands are available at 557, 1013, 1348, 1664 and 3209 cm^{-1}. The 557 cm^{-1} band is referring to the Mo–S bonds in the MoS_2 sample whereas the 1013 cm^{-1} band is indicating S–S bonds. The existence of hydroxyl group and Mo–O bonds including the stretching vibrations contributes to the 1348 and 1664 cm^{-1} absorption bands. Stretching vibration can also be owing to the present hydroxyl group, by the peak at 3209 cm^{-1} [39]. Curve (c) demonstrates the Map-6 nanoparticles FTIR spectra. There are

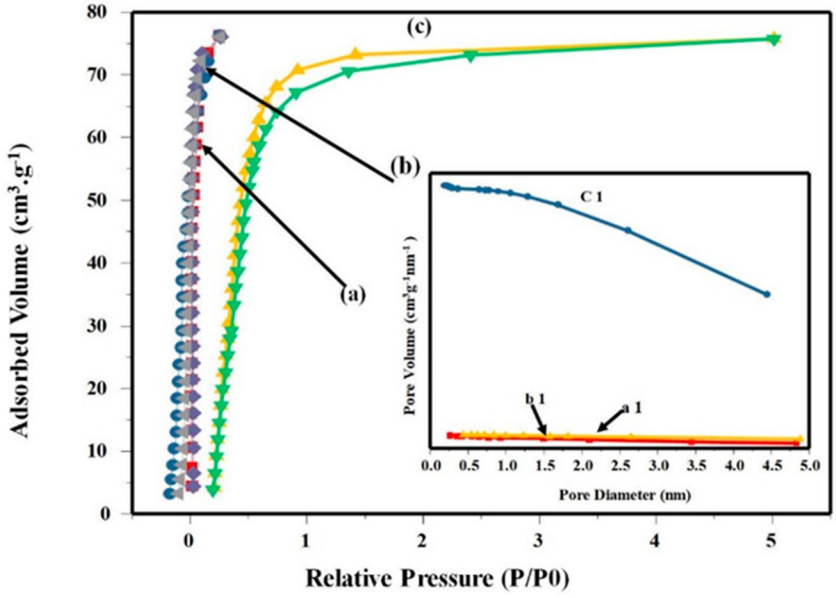

Figure 5. N_2 adsorption–desorption isotherms of (a) Ag_3PO_4, (b) MoS_2, (c) MAP-6, the inset is the pore size distribution curves (a1) Ag_3PO_4, (b1) MoS_2, (c1) MAP-6.

absorption bands at 553, 841, 1014, 1384, 1430, 1662, 2882 and 3225 cm^{-1}.

A band at 553–841 cm^{-1} is referring to the presence of aromatic halide. The medium to strong bands observed in the range 1014–1430 cm^{-1} are assigned to C–O stretching vibrations and the value of C=N stretching vibration is found 1650–1690 cm^{-1}. Consequently, the OH vibration of the phenolic proton appears as a broad band in the region 3202–3234 cm^{-1} possibly due to the overlapping of the symmetric and antisymmetric OH stretching vibrations of lattice water [41–44]. The bands are due to the hydroxyl groups and water molecules adsorbed on the Ag_3PO_4 and MoS_2 surface. The photocatalytic reaction for the oxidation as well as reduction may develop a relationship between contaminants and hydroxyl free radicals.

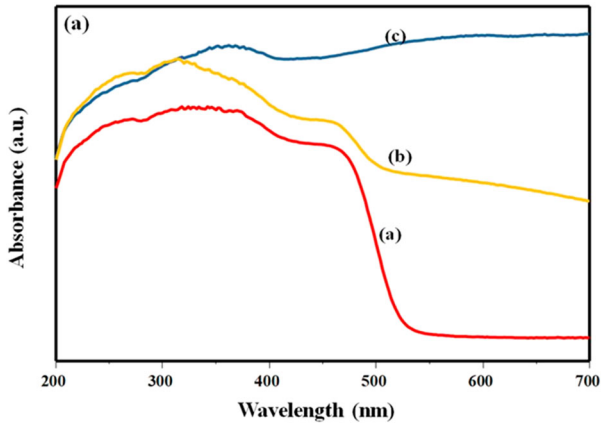

Figure 6. UV–Vis spectra of (a) Ag_3PO_4, (b) MoS_2 and (c) MAP-6.

3.3.6. Photoluminescence analysis

To realize its larger photocatalytic activity of the MAP-6 composites comparative to both the pure Ag_3PO_4 and MoS_2 nanosheets, the photoluminescence (PL) investigation was used to calculate the recombination, transfer and mitigation mechanisms of a photogenerated electron–hole pairs in the photocatalyst samples as-prepared. A lower PL intensity generally indicates a lower recombination of charge carriers, leading to larger photocatalytic activity. As indicated in Figure 10(a), it can be seen that the pure Ag_3PO_4 sample has a major emission peak at approximately 533 nm, which corresponds to its broadband gap and that the recombination

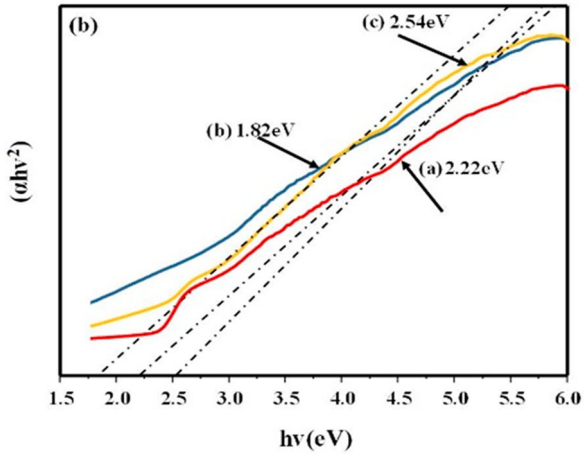

Figure 7. Evaluation of the band gap energies of (a) Ag_3PO_4, (b) MoS_2 and (c) MAP-6 photocatalyst.

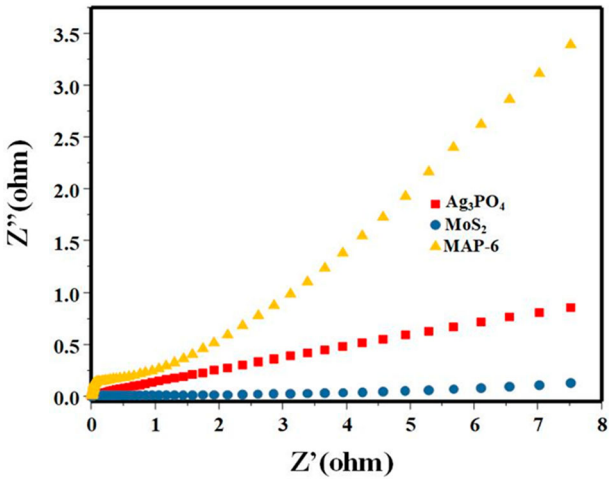

Figure 8. EIS Nyquist plots of pure Ag_3PO_4, MoS_2 and MAP-6 photocatalyst.

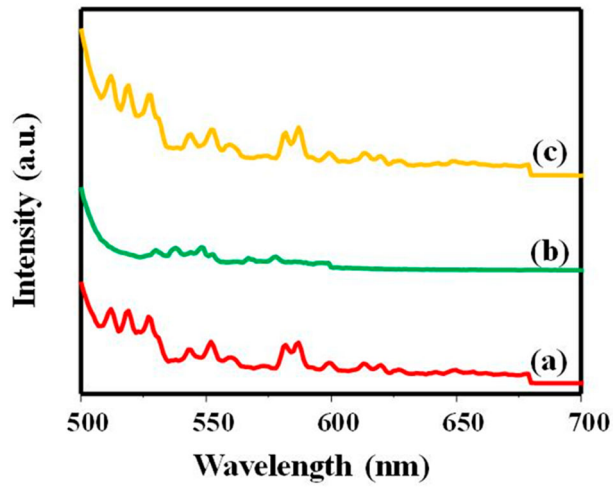

Figure 10. Photoluminescence spectra of (a) Ag_3PO_4, (b) MoS_2 nanosheet, (c) MAP-6 composite.

electron–hole pairs specifically imply a cluster-to-cluster transition of charge.

In Figure 10(b), the MoS_2 nanosheet shows only one broadband of absorption band that can be due to the mixed optical absorption by direct and indirect band transitions in narrower and thicker MoS_2 layers. The excitations occur due to direct transition that generates two noticeable PL peaks in the nanosheets of MoS_2 between the top of the valance band edge and bottom of the conduction band, at about ~600 and ~525 nm, respectively. It displays a similar spectrum of PL about ~545 nm (Figure 10b), equivalent to a 1.82 eV band gap from the relaxation of direct nanosheet excitations in MoS_2. Hence, significant PL intensity is detected in the MoS_2 nanosheet owing to direct band gap nature, favouring direct electronic transition. An identical PL spectrum is attained after the introduction of the MoS_2 nanosheet; moreover, the general emission intensity is definitely decreased relative to that of pure Ag_3PO_4, indicating that the formation of a heterojunction among Ag_3PO_4 and MoS_2 nanosheet suppresses the recombination of the photoexcited electron–hole on the Ag_3PO_4, surface. The finding from PL study shows that the MoS_2 nanosheet with a two-dimensional π-conjugated structure possibly will assist as an efficient electron-accepting material and also that close interaction among Ag_3PO_4 and MoS_2 nanosheet. It will boost the separation of hole pairs under solar light irradiation and afterwards electrons easily be transferred to MoS_2 nanosheet, which inhibits the direct transition of electrons and holes recombination.

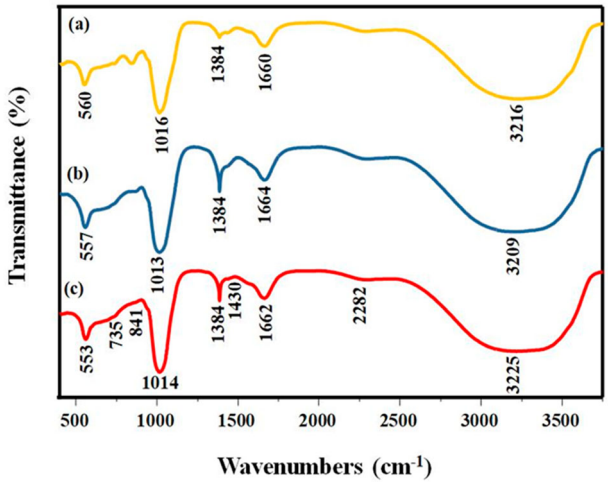

Figure 9. FTIR spectra of (a) Ag_3PO_4, (b) MoS_2 and (c) MAP-6 composites.

A charge separating is generally credited to a charge transfer at the interface by combined photocatalysts, including driving force resulting from the corresponding band potentials of the two components. The PL emission intensity and photocatalytic performance are adversely affected. The lowest level of PL emissions but the highest photocatalytic activity is shown in Figure 10(c). Almost all UV–vis absorption and PL spectrum imply that the MoS_2 nanosheet is more exciting in the same circumstances and that it can play an important role in increasing the efficiency of photocatalytic degradation.

3.4. Photocatalytic activity

Photocatalytic performance of the different ratios of synthesized MAP-6, MoS_2 and Ag_3PO_4 is shown in Figure 11 (a) and evaluated by the degradation of TCH. Blank experiment (no catalyst) was also conducted under visible light condition. TCH of self-degradation was insignificant without catalyst (Figure 11a). It stated clearly that TCH's self-degradation under visible light

irradiation is negligible. The degradation efficiency of MAP-6 was compared with pure Ag_3PO_4 (66%) and MoS_2 (48.9%), and resultant significantly improved. In addition, factually, MAP-6 demonstrated degradation performance up to 70.7% for TCH after 10 min irradiation. Attempting to make use of the benefits of MAP-6 has outstanding photocatalytic performance and 80.50% degradation efficiency.

The photocatalytic activity of the different ratios of photocatalyst on the degradation of TCH is approximately in contract through the Langmuir–Hinshelwood pseudo-first-order reaction procedure: ln $(C_0/C_t) = k_t$. As per finding of the kinetic study conclusion (Figure 11b), the graph of ln (C_0/C_t) versus time (t) provides a straight line. The kinetic constant (k) for the pure MoS_2, Ag_3PO_4, MAP-1, MAP-2, MAP-3, MAP-4, MAP-5, MAP-6 and MAP-7 are 0.0168, 0.0269, 0.0084, 0.0254, 0.0195, 0.0322, 0.0385, 0.0409 and 0.0316, respectively. Undoubtedly, the kinetic constant (k) of MAP-6 for TCH degradation is corresponding to 0.0409, which are significantly

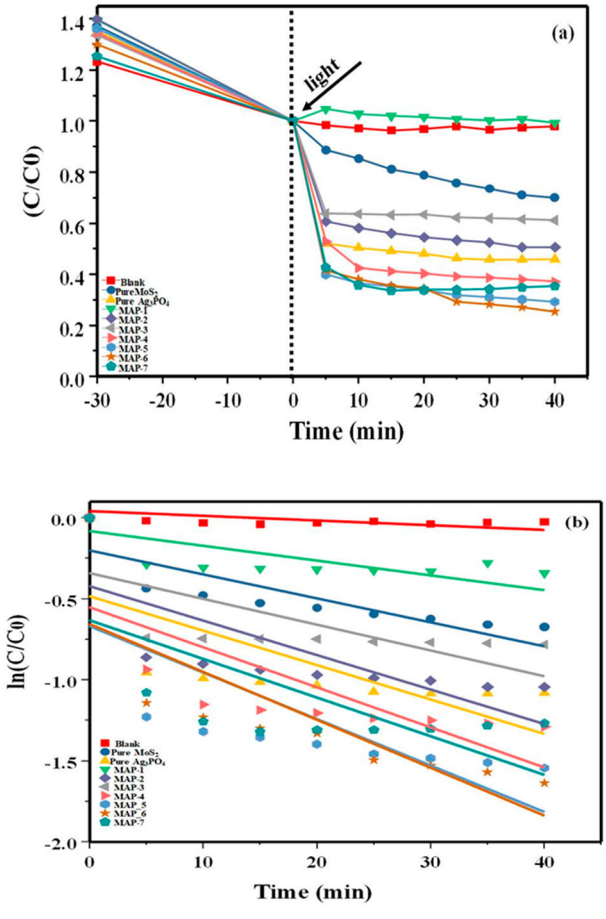

Figure 11. (a) Photocatalytic activities and performance were carried out of the obtained samples for TCH degradation under visible light irradiation. (b) Comparison by visible light irradiation of apparent rate constants (k) of the acquired samples for TCH degradation.

greater than Ag_3PO_4 (0.0269) and MoS_2 (0.0168). Moreover, photocatalytic performance and photocatalyst stability are also essential for practical application. Thus the stability of the photocatalytic materials has been investigated. As displayed in Figure 12, the photodegradation efficiency of TCH after four cycling tests shows a slight decrease, representing that the prepared MAP-6 was stable and efficient for the degradation of TCH in water under visible light.

3.5. Photocatalytic degradation mechanism

The main active species during most of the photocatalytic system was established by reactive oxide trapping tests. The use of $\bullet O_2^-$ radicals, h^+, and $^{\bullet}OH$ radicals as a scavenger, respectively, was carried out from *p*-benzoquinone (BQ, 0.0001 mol/L), disodium ethylene diamine tetra acetate (EDTA, 0.01 mol/L) and isopropanol (IPA,0.01 mol/L). Until radiation exposure in three isolated environments, scavengers were applied to the persistent organic antibiotic solution. TCH was consumed as the main pollutant in this segment. Adsorbing potential (q_e) and degradation efficiency (E) were determined using the corresponding formulae [45–49]:

$$q_e = \frac{(C_0 - C_e)V}{W} \text{ and } E(\%) = \frac{C_0 - C_e}{C_0} \times 100,$$

in which C_0 represents initial concentration of the determined antibiotic solution (g/L), equilibrium concentration after degradation/ adsorption (g/L) denoted with C_e, where W and V represent the mass of the photocatalyst (g) and volume of persistent antibiotic solution (mL), respectively. Figure 13 displays the principal active photocatalytic degradation species of TCH.

During this procedure, the photocatalysis of TCH decreased significantly with IPA and TEOH build up and revealed the minor part of the reaction under solar light to holes (h^+) and BQ supplements reduced to some extent decreased and prevented the effect of degradation.

Additionally, the valence band (VB) and conduction band (CB) band edge positions also have an important impact upon the redox catalytic activity. It can be determined from the following equation: $E_{VB} = \chi - E_e + 0.5E_g$ and $E_{CB} = E_{VB} - E_g$, where E_{VB} and E_{CB} stand for VB and CB edge potentials, respectively; semiconductor electronegativity is denoted by 'χ', therefore, it represents the constituent atoms electronegativity. The Ag_3PO_4 and MoS_2 have χ-values 5.96 and 5.32 eV, respectively. The hydrogen scale free electron energy is denoted by E_e and its value is around 4.5 eV. E_g was represented as

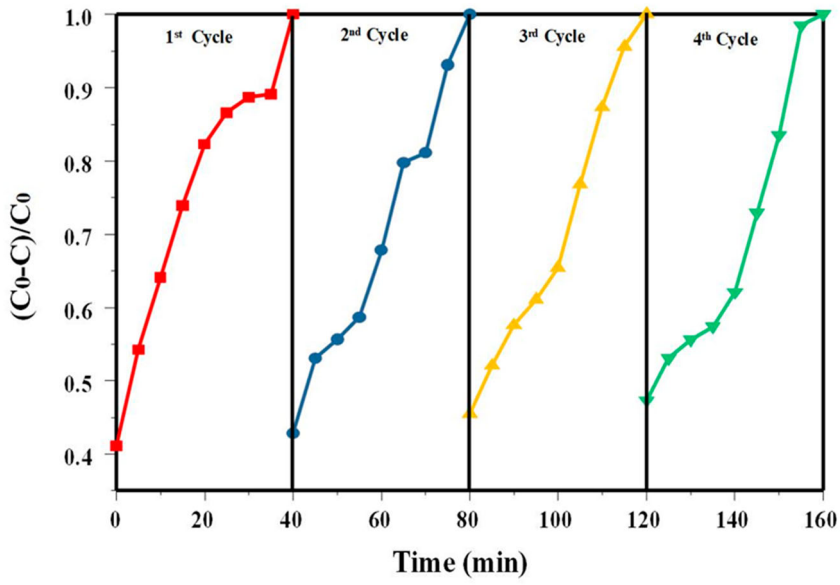

Figure 12. Photocatalytic activities of MAP-6 composite during the recycling experiments.

the semiconductor band gap energy and its values for Ag_3PO_4 and MoS_2 are approximately 2.22eV and 1.82eV, respectively [50–52].

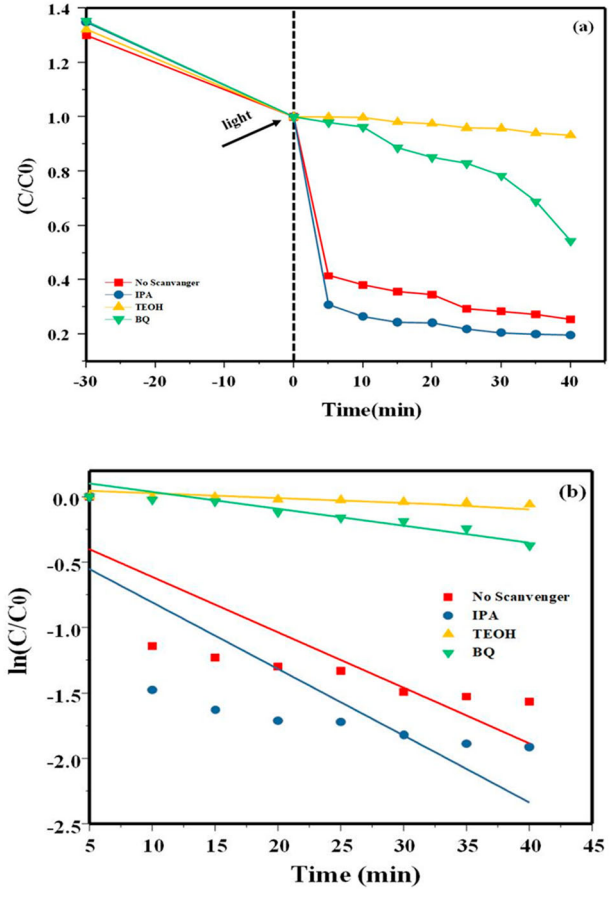

Figure 13. Influence of various scavenger adding on the photocatalytic degradation of TCH under visible light.

The EVB values of Ag_3PO_4 and MoS_2 are measured at about 2.57 and 1.73 eV, the lowest of which is more favourably for both Ag_3PO_4 and MoS_2 than the O_2/H_2O redox (1.23eV), both of which can potentially separate water in oxygen. The experimental calculation indicates that the E_{VB} values of Ag_3PO_4 and MoS_2 are measured at about 2.57 and 1.73 eV, the topmost of which is more favourable for both Ag_3PO_4 and MoS_2 than the O_2/H_2O (1.23eV), that is more positive than the redox potential of O_2/H_2O (1.23eV), theoretically, both semiconductors can have ability to produce oxygen by splitting water. Nevertheless, for practical water splitting using solar energy, Ag_3PO_4 perform as the oxygen-developing catalyst due to its large positive potential than that oxidation potential of water. Consequently, Ag_3PO_4 and MoS_2 E_{CB} positions are determined to be about at 0.35 and −0.09 eV, respectively. The photocatalytic process is preliminary and schematically demonstrated in Figure 14, which is based on the arguments above about the photogenerated degradation of TCH over the MoS_2/Ag_3PO_4 (MAP-6) composites. All Ag_3PO_4 and MoS_2 nanosheets can be effectively excited by visible light irradiation, resulting the generation of photogenerated electron–hole pairs, and these photogenerated electrons exited from top of VB of Ag_3PO_4 and MoS_2 may easily be transferred to the bottom of their conforming CB of Ag_3PO_4 and MoS_2, respectively. Simultaneously, nanoparticles generated at the interface of Ag_3PO_4 and MoS_2, which was corresponding to metallic Ag nanoparticles create through the photo corrosion of Ag_3PO_4 and act as the carrier separation centre to configure with the visible light-driven MoS_2/Ag_3PO_4 Z-scheme system. The dangling

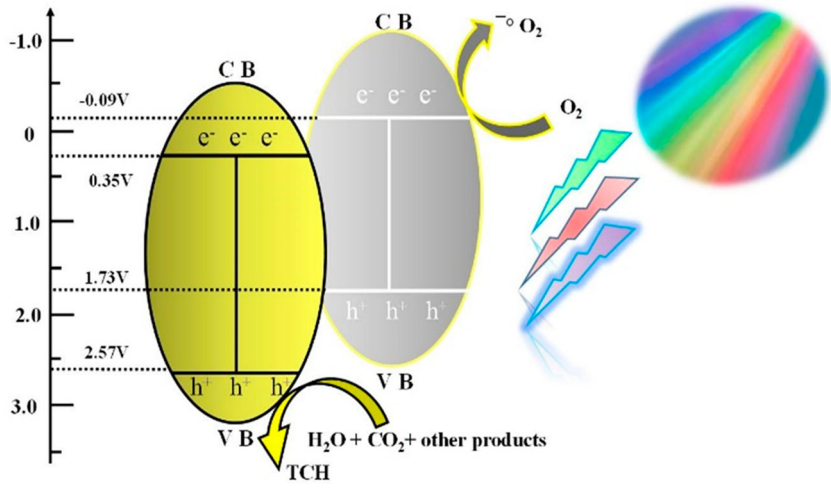

Figure 14. Schematic diagram of photocatalytic degradation of TCH under visible light irradiation by MAP-6 composite in visible light conditions.

bond photoelectrons of Ag_3PO_4 form the CB may simply change into nanoparticles over the Schottky barrier because Ag has additional positive Fermi energy as compared to the Ag_3PO_4 CB energy level. At the same time, MoS_2 holes in the VB can furthermore transport to metallic Ag nanoparticles, nevertheless, these photo-induced electron and hole pairs may annihilate at the surface of Ag.

In the meantime, the conduction band of MoS_2 accommodates reductive photoelectrons, and on the other side valence band of Ag_3PO_4 will assist strong oxidizing holes. The Ag_3PO_4 holes would oxidize TCH directly through photocatalysis process, while MoS_2 high reduction electrons would react with O_2 to form $O_2^{\bullet-}$, which could promote oxidizing of TCH. Consequently, the successful advancement of organic pollutant photodegradation can be continued efficiently. Furthermore, the procedure can be defined as follows:

$$MoS_2/Ag_3PO_4 + h\upsilon \rightarrow MoS_2(h^+ + e^-) + Ag_3PO_4(h^+ + e^-)$$
$$MoS_2(e^-) + O_2 \rightarrow MoS_2 + O_2^{\bullet-}$$
$$Ag_3PO_4(h^+) + H_2O/^{-}OH \rightarrow Ag_3PO_4 + {}^{\bullet}OH$$
$$O_2^{\bullet-} + TCH \rightarrow \text{oxidation products}$$
$$Ag_3PO_4(h^+) + TCH \rightarrow Ag_3PO_4 + \text{oxidation product}$$

The photogenerated charge carriers are spatially separated, that significantly prevents the recombination of photogenerated electrons and holes, according to the Z-scheme charge-carrier transfer process. This enhances the photogenerated carrier's oxidation and reduction capability and enhances the photogenerated carrier's lifespan of Ag_3PO_4 holes and photogenerated MoS_2 electrons, thus strengthening the photocatalytic capacity.

4. Conclusion

In conclusion, the effective MoS_2 ultrathin nanosheets/Ag_3PO_4 composite photocatalysts were effectively synthesized by the microwave assisted hydrothermal process and Ag_3PO_4 particle size in contact with the MoS_2 ultrathin nanosheets was found to be significantly reduced and exfoliated MoS_2 as a good support for the photocatalyst. MoS_2/Ag_3PO_4 (MAP-6) has an excellent photocatalytic activity. The MoS_2/Ag_3PO_4 (MAP-6) composites show remarkable photocatalytic activity and consistency for aqueous TCH solution, under visible light irradiation. The doping of dispersed MoS_2 ultrathin nanosheets developed the construction of Z-scheme MoS_2/Ag_3PO_4 heterojunction that owns large productivity of carrier transportation and separation, and also has stronger reduction and oxidation ability for the persistent organic pollutants. The theoretical experimental characterization analysis of band structures recommended that to enhance oxidation efficiency of water is attributed to significant visible light harvesting, more effective charge transportation. The photocatalytic action of MAP-6 nanocomposite was more advanced as compared to MoS_2 ultrathin nanosheet and Ag_3PO_4 nanoparticles, individually, for the photocatalytic deterioration of persistent organic pollutants like TCH under visible light and improved the parting of photogenerated electrons and holes. In addition, superoxide radicals ($^{\bullet}O_2^-$) revealed the significant effect on the photocatalytic deterioration of TCH. We were studied for determining the activity of the composites by photocatalytic degradation of TCH toxic antibiotic as a standard pollutant under visible light irradiation. The results of the study show that the photocatalytic system MoS_2/Ag_3PO_4 (MAP-6) is look forwarded to act as an

encouraging visible light photocatalyst for wastewater remediation contaminated with real-world organic factory pollutants.

Acknowledgements

The financial supports to this work from the National Natural Science Foundation of China (Nos. 51974216, 51704212 and 51704220), the Natural Science Foundation of Hubei Province (No. 2019CFB536) are gratefully acknowledged.

Disclosure statement

No potential conflict of interest was reported by the author(s).

Funding

The financial supports to this work from the National Natural Science Foundation of China [grant number 51974216], [grant number 51704212] and [grant number 51704220], the Natural Science Foundation of Hubei Province [grant number 2019CFB536] are gratefully acknowledged.; Wuhan University of Technology.

References

[1] Huang H, Song Z, Wei N, et al. Ultrafast viscous water flow through nanostrand-channelled graphene oxide membranes. Nat Commun. 2013;4.

[2] Sun H, Li A, Qin X, et al. Three-dimensional superwetting mesh film based on graphene assembly for liquid transportation and selective absorption. ChemSusChem. 2013;6:2377–2381.

[3] Rivera-Utrilla J, Prados-Joya G, Sánchez-Polo M, et al. Removal of nitroimidazole antibiotics from aqueous solution by adsorption/bioadsorption on activated carbon. J Hazard Mater. 2009;170:298–305.

[4] Watkinson AJ, Murby EJ, Kolpin DW, et al. The occurrence of antibiotics in an urban watershed: from wastewater to drinking water. Sci Total Environ. 2009;407:2711–2723. doi:10.1016/j.scitotenv.2008.11.059.

[5] Ji L, Chen W, Duan L, et al. Mechanisms for strong adsorption of tetracycline to carbon nanotubes: A comparative study using activated carbon and graphite as adsorbents. Environ Sci Technol. 2009;43:2322–2327.

[6] Zhang Z, Lan H, Liu H, et al. Removal of tetracycline antibiotics from aqueous solution by amino-Fe (III) functionalized SBA15. Colloids Surf A. 2015;471:133–138. doi:10.1016/j.colsurfa.2015.02.018.

[7] Hong PY, Al-Jassim N, Ansari MI, et al. Environmental and public health implications of water reuse: antibiotics, antibiotic resistant bacteria, and antibiotic resistance genes. Antibiotics. 2013;2:367–399.

[8] Aristilde L, Marichal C, Miéhé-Brendlé J, et al. Interactions of oxytetracycline with a smectite clay: a spectroscopic study with molecular simulations. Environ Sci Technol. 2010;44:7839–7845.

[9] Hu W, Peng C, Luo W, et al. Graphene-based antibacterial paper. ACS Nano. 2010;4:4317–4323.

[10] Ai L, Jiang J. Removal of methylene blue from aqueous solution with self-assembled cylindrical graphene-carbon nanotube hybrid. Chem Eng J. 2012;192:156–163. doi:10.1016/j.cej.2012.03.056.

[11] Kim SH, Shon HK, Ngo HH. Adsorption characteristics of antibiotics trimethoprim on powdered and granular activated carbon. J Ind Eng Chem. 2010;16:344–349. doi:10.1016/j.jiec.2009.09.061.

[12] Moussavi G, Alahabadi A, Yaghmaeian K, et al. Preparation, characterization and adsorption potential of the NH_4Cl^- induced activated carbon for the removal of amoxicillin antibiotic from water. Chem Eng J. 2013;217:119–128. doi:10.1016/j.cej.2012.11.069.

[13] Dong S, Feng J, Fan M, et al. Recent developments in heterogeneous photocatalytic water treatment using visible light-responsive photocatalysts: a review. RSC Adv. 2015;5:14610–14630. doi:10.1039/C4RA13734E.

[14] Li X, Yu J, Low J, et al. Engineering heterogeneous semiconductors for solar water splitting. J Mater Chem A. 2015;3:2485–2534. doi:10.1039/C4TA04461D.

[15] Yue D, Qian X, Zhao Y. Photocatalytic remediation of ionic pollutant. Science Bulletin. 2015;60:1791–1806. doi:10.1007/s11434-015-0918-5.

[16] Chen J, Qiu F, Xu W, et al. Recent progress in enhancing photocatalytic efficiency of TiO_2-based materials. Appl Catal, A. 2015;495:131–140. doi:10.1016/j.apcata.2015.02.013.

[17] Haibo O, Jianfeng H, Xierong Z, et al. Visible-light photocatalytic activity of SiC hollow spheres prepared by a vapor-solid reaction of carbon spheres and silicon monoxide. Ceram Int. 2014;40:2619–2625. doi:10.1016/j.ceramint.2013.10.068.

[18] Song X, Hu Y, Zheng M, et al. Solvent-free in situ synthesis of g-C_3N_4/{001}TiO_2 composite with enhanced UV- and visible-light photocatalytic activity for NO oxidation. Appl Catal, B. 2016;182:587–597. doi:10.1016/j.apcatb.2015.10.007.

[19] Yue Q, Wan Y, Sun Z, et al. Mop is a novel, noble-metal-free cocatalyst for enhanced photocatalytic hydrogen production from water under visible light. J Mater Chem A. 2015;3:16941–16947.

[20] Casbeer E, Sharma VK, Li XZ. Synthesis and photocatalytic activity of ferrites under visible light: a review. Sep Purif Technol. 2012;87:1–14. doi:10.1016/j.seppur.2011.11.034.

[21] Peng B, Ang PK, Loh KP. Two-dimensional dichalcogenides for light-harvesting applications. Nano Today. 2015;10:128–137. doi:10.1016/j.nantod.2015.01.007.

[22] Takata T, Pan C, Domen K. Recent progress in oxynitride photocatalysts for visible-light-driven water splitting. Sci Technol Adv Mater. 2015;16:033506.

[23] Bloh JZ, Dillert R, Bahnemann DW. Designing optimal metal-doped photocatalysts: correlation between photocatalytic activity, doping ratio, and particle size. J Phys Chem C. 2012;116:25558–25562.

[24] Gyawali G, Adhikari R, Joshi B, et al. Sonochemical synthesis of solar-light-driven Aǧ–$PbMoO_4$ photocatalyst. J Hazard Mater. 2013;263:45–51. doi:10.1016/j.jhazmat.2013.03.065.

[25] Adhikari R, Gyawali G, Kim TH, et al. EDTA mediated microwave hydrothermal synthesis of WO_3 hierarchical structure and its photoactivity under simulated solar

light. J Environ Chem Eng. 2014;2:1365–1370. doi:10.1016/j.jece.2014.02.019.
[26] Kim TH, Rodríguez-González V, Gyawali G, et al. Synthesis of solar light responsive Fe, N co-doped TiO_2 photocatalyst by sonochemical method. Catal Today. 2013;212:75–80. doi:10.1016/j.cattod.2012.09.014.
[27] Lee HS, Min SW, Chang YG, et al. Mos_2 nanosheet phototransistors with thickness-modulated optical energy gap. Nano Lett. 2012;12:3695–3700.
[28] Li H, Wu J, Yin Z, et al. Preparation and applications of mechanically exfoliated single-layer and multilayer MoS_2 and WSe_2 nanosheets. Acc Chem Res. 2014;47:1067–1075.
[29] Coleman JN, Lotya M, O'Neill A, et al. Two-dimensional nanosheets produced by liquid exfoliation of layered materials. Science. 2011;331:568–571.
[30] Huang Y, Miao YE, Zhang L, et al. Synthesis of few-layered MoS_2 nanosheet-coated electrospun SnO_2 nanotube heterostructures for enhanced hydrogen evolution reaction. Nanoscale. 2014;6:10673–10679. doi:10.1039/C4NR02014F.
[31] Yang X, Liu W, Xiong M, et al. Au nanoparticles on ultrathin MoS_2 sheets for plasmonic organic solar cells. J Mater Chem A. 2014;2:14798–14806. doi:10.1039/C4TA03178D.
[32] Liu X, Li L, Wei Y, et al. Facile synthesis of boron- and nitride-doped MoS_2 nanosheets as fluorescent probes for the ultrafast, sensitive, and label-free detection of Hg^{2+}. Analyst. 2015;140:4654–4661.
[33] Chen Z, Cummins D, Reinecke BN, et al. Core–shell MoO_3–MoS_2 nanowires for hydrogen evolution: a functional design for electrocatalytic materials. Nano Lett. 2011;11:4168–4175.
[34] Wu X, Yan X, Dai Y, et al. Facile synthesis of AgNPs/MoS_2 nanocomposite with excellent electrochemical properties. Mater Lett. 2015;152:128–130. doi:10.1016/j.matlet.2015.03.118.
[35] Vattikuti SVP, Byon C. Synthesis and characterization of molybdenum disulfide nanoflowers and nanosheets: nanotribology. J Nanomater. 2015;2015.
[36] Li H, Yu K, Lei X, et al. Synthesis of the MoS_2@CuO heterogeneous structure with improved photocatalysis performance and H_2O adsorption analysis. Dalt Trans. 2015;44:10438–10447.
[37] Wang L, Chai Y, Ren J, et al. Ag_3PO_4 nanoparticles loaded on 3D flower-like spherical MoS_2: a highly efficient hierarchical heterojunction photocatalyst. Dal. Trans. 2015;44:14625–14634.
[38] Peng WC, Wang X, Li XY. The synergetic effect of MoS_2 and graphene on Ag_3PO_4 for its ultra-enhanced photocatalytic activity in phenol degradation under visible light. Nanoscale. 2014;6:8311–8317.
[39] Zhan W, Yuan Y, Yang B, et al. Construction of MoS_2 nanoheterojunction via ZnS doping for enhancing in-situ photocatalytic reduction of gold thiosulfate complex. Chem Eng J. 2020;394:124866. doi:10.1016/j.cej.2020.124866.
[40] Zhan W, Jia F, Yuan Y, et al. Controllable incorporation of oxygen in MoS_2 for efficient adsorption of Hg^{2+} in aqueous solutions. J Hazard Mater. 2020;384:121382. doi:10.1016/j.jhazmat.2019.121382.
[41] Manibalan G, Murugadoss G, Thangamuthu R, et al. Enhanced photocatalytic activity of CeO_2@α-MoO_3 heterostructure. J Mater Sci: Mater Electron. 2018;29:13692–13702.
[42] Manibalan G, Murugadoss G, Thangamuthu R, et al. High electrochemical performance and enhanced electrocatalytic behavior of a hydrothermally synthesized highly crystalline heterostructure CeO_2@NiO nanocomposite. Inorg Chem. 2019;58:13843–13861.
[43] Murugadoss G, Thangamuthu R, Rajesh Kumar M. Formamidinium lead iodide perovskite: structure, shape and optical tuning via hydrothermal method. Mater Lett. 2018;231:16–19. doi:10.1016/j.matlet.2018.08.003.
[44] Murugadoss G, Thangamuthu R, Senthil Kumar SM, et al. Synthesis of ligand-free, large scale with high quality all-inorganic $CsPbI_3$ and $CsPb_2Br_5$ nanocrystals and fabrication of all-inorganic perovskite solar cells. J Alloys Compd. 2019;787:17–26. doi:10.1016/j.jallcom.2019.02.018.
[45] Pirhashemi M, Habibi-Yangjeh A. Ultrasonic-assisted preparation of plasmonic ZnO/Ag/Ag_2WO_4 nanocomposites with high visible-light photocatalytic performance for degradation of organic pollutants. J Colloid Interface Sci. 2017;491:216–229. doi:10.1016/j.jcis.2016.12.044.
[46] Pirhashemi M, Habibi-Yangjeh A. Zno/$NiWO_4$/Ag_2CrO_4 nanocomposites with p-n-n heterojunctions: highly improved activity for degradations of water contaminants under visible light. Sep Purif Technol. 2018;193:69–80. doi:10.1016/j.seppur.2017.11.007.
[47] Kumar MR, Murugadoss G, Pirogov AN, et al. A facile one step synthesis of SnO_2/CuO and CuO/SnO_2 nanocomposites: photocatalytic application. J Mater Sci: Mater Electron. 2018;29:13508–13515.
[48] Urusova N, Kumar MR, Semkin M, et al. Crystal structure and magnetic properties of Sr_2Ni_1-xMgxMoO$_6$ (x = 0, 0.25, 0.5, and 0.75) polycrystals. Solid State Sci. 2020;99:106008.
[49] Yu ZJ, Kumar MR, Sun DL, et al. Large scale production of hexagonal ZnO nanoparticles using PVP as a surfactant. Mater Lett. 2016;166:284–287.
[50] Yu ZJ, Kumar MR, Chu Y, et al. Photocatalytic decomposition of RhB by newly designed and highly effective CF@ZnO/CdS hierarchical heterostructures. ACS Sustain Chem Eng. 2018;6:155–164.
[51] Zarezadeh S, Habibi-Yangjeh A, Mousavi M. BiOBr and AgBr co-modified ZnO photocatalyst: A novel nanocomposite with p-n-n heterojunctions for highly effective photocatalytic removal of organic contaminants. J Photochem Photobiol A. 2019;379:11–23. doi:10.1016/j.jphotochem.2019.05.013.
[52] Zarezadeh S, Habibi-Yangjeh A, Mousavi M. Fabrication of novel ZnO/BiOBr/C-Dots nanocomposites with considerable photocatalytic performances in removal of organic pollutants under visible light. Adv Powder Technol. 2019;30:1197–1209. doi:10.1016/j.apt.2019.03.016.